






Thermomechanical Modeling of Laser Ablation Therapy of Tumors: Sensitivity Analysis and Optimization of Influential Variables

Ahad Mohammadi , Leonardo Bianchi , Sanzhar Korganbayev , Martina De Landro , and Paola Saccomandi 

Abstract—In cancer treatment, laser ablation is a promising technique used to induce localized thermal damage. Different variables influence the temperature distribution in the tissue and the resulting therapy efficacy; thus, the optimal therapy settings are required for obtaining the desired clinical outcome. In this work, thermomechanical modeling of contactless laser ablation was implemented to analyze the sensitivity of independent variables on the optimal treatment conditions. The Finite Element Method was utilized to solve the governing equations, i.e., the bio-heat, mechanical deformation, and the Navier-Stokes equations. Validation of the model was performed by comparing experimental and simulated temperatures, which indicated high accuracy for estimating temperature. In particular, the results showed that the model can estimate temperature with a good correlation factor ($R = 0.98$) and low Mean Absolute Error ($3.9\text{ }^\circ\text{C}$). A sensitivity analysis based on laser irradiation time, power, beam distribution, and the blood vessel depth on temperature distribution and fraction of necrotic tissue was performed. An optimization process was performed based on the most significant variables, i.e., laser irradiation time and power. This resulted in an indication of the optimal therapy settings for achieving maximum procedure efficiency i.e., the required fraction of necrotic tissue within the target volume, constituted by tumor and safety margins around it.

Index Terms—Laser ablation, bioheat transfer, physical deformation, mathematical modeling, liver tissue.

NOMENCLATURE

A	Frequency factor for the kinetic expression (1/s)
a	Absorption coefficient (1/m)
b	Scattering coefficients (1/m)
c	Anisotropy coefficients (1/m)
B	Scattering coefficient (1/m)
C	Heat capacity of tissue (J/kg K)

C_b	Specific heat capacity of blood (J/kg K)
C_m	Effective specific heat
E	Activation energy for irreversible damage reaction (J/mol)
h_{am}	Convective coefficient of the air
I	Irradiation intensity (W/m^2)
K	Thermal conductivity of the tissue
N	Poisson's ratio
R	Universal gas constant
T	Tissue temperature ($^\circ\text{C}$)
T_{am}	Ambient temperature
T_b	T_b is the temperature of blood ($^\circ\text{C}$)
T_{ref}	Reference temperature
U	Average displacement (m)
W	Tissue water content
Q_E	Water vaporization heat
Q_{laser}	Laser Heat
$Q_{metabolic}$	Metabolic heat
Z	Depth of the tissue

Greek symbols

α	Tissue thermal expansion coefficient ($1/^\circ\text{C}$).
ε	Strain
Ω	Degree of damaged tissue
θ	Degree of tissue injury
Σ	Width of the irradiated area (mm)
ε	Surface emissivity
Σ	Setfan–Boltzmann constant
ω_b	Blood perfusion rate (1/s).
ω_0	Initial perfusion rate (1/s).
ρ_b	The density of blood (kg/m^3)
ρ_{tissue}	The density of tissue (kg/m^3)
μ_{eff}	Effective attenuation coefficient (1/m)
δ_{ij}	Kronecker delta
θ	Temperature excess over the ambient
λ	Lame's constant
μ	Modulus of rigidity
β	Second order tensor of thermoelastic moduli

I. INTRODUCTION

THE development of laser technology applications in the medical field has stimulated its widespread use to treat

Manuscript received December 3, 2020; revised April 3, 2021 and May 31, 2021; accepted June 18, 2021. Date of publication June 28, 2021; date of current version December 23, 2021. This work was supported by the European Research Council (ERC) under the European Union's Horizon 2020 research and innovation programme under Grant Agreement 759159. (Corresponding author: Ahad Mohammadi.)

Ahad Mohammadi is with the Department of Mechanical Engineering, Politecnico di Milano, 20156 Milano, Italy (e-mail: ahad.mohammadi@polimi.it).

Leonardo Bianchi, Sanzhar Korganbayev, Martina De Landro, and Paola Saccomandi are with the Department of Mechanical Engineering, Politecnico di Milano, Italy.

Digital Object Identifier 10.1109/TBME.2021.3092889

cancer [1], [2]. The laser energy delivered to the target is absorbed and converted into thermal energy; thus, a localized thermal effect that brings coagulation and consequent necrosis of the malignant tissue is achieved for therapeutic purposes. Due to the increasing demand for reliability and safety of this approach, the prediction of tissue behavior during laser-induced treatment (i.e., laser ablation, LA) is of paramount importance. Indeed, several factors influence LA outcome, including laser light wavelength, laser power and treatment time [3], mechanical, thermal, and optical properties of the tissue [4], presence and amount of blood flow [5], and the applicator optical emission characteristics [6]. In this context, the influential variables should be optimized by maximizing the therapeutic effect and minimizing unwanted side effects in the healthy surrounding tissue. Sophisticated techniques have been proposed for predicting thermal therapy outcomes, and the majority of them are based on numerical calculation [7].

An important aspect when predicting the outcome of LA is the inclusion of thermal-dependent physical properties of the tissue and the phase change occurrence due to water vaporization at the therapeutic temperatures.

Yang *et al.* (2007) proposed a new method to study tissue ablation using a modified bioheat diffusion equation. They added an extra term to the bioheat equation to obtain an effective and temperature-dependent specific heat, and used a numerical method for microwave ablation of the bovine liver [8]. This model has been recently compared by S. Blauth *et al.* (2020) to an enthalpy model, which uses an additional state equation to model the phase transition [9] and validated during *ex vivo* experiments.

Another key factor in the heat transfer analysis inside biological tissues is blood perfusion, which can strongly affect the therapy efficacy due to the heat-sink effect. Shih *et al.* (2006) focused on the cooling effects of thermally significant blood vessels. Their results show that the short duration and high-intensity heating effectively cover the treated tumor inside with a blood vessel 200 μm in diameter; also, with a diameter larger than 2 mm, the longer heating duration and higher heating power density are not sufficient for complete necrosis of the tumor. Besides, suppose more energy is delivered into the heated target. In that case, the significant cooling effect of the blood vessels is still strong. It then may cause a pronounced overheating of the surrounding normal tissue, especially near the downstream of blood vessels [10]. Shirkavand and Nazif (2019) proposed a 3D forearm model based on anthropometric measurement. This research indicates that decreasing the body metabolism, increasing the blood perfusion rate, and using a fluctuating heat flux can present hyperthermia without causing damage such as burn injuries to other tissue parts. Also, blood perfusion on the tissue temperature distribution is not significantly affected by the type of external heat source [11].

In addition, the exposure of tissues to the high temperature involved in the thermal therapies results in thermally-induced deformations. It has been demonstrated that this phenomenon also can affect physiological mechanisms and energy distributions in the tissue [12], [13]. Whereas several works have focused on the numerical modeling of the thermal effect only,

mechanical deformations within the numerical models are relatively recent, with limited results for LA in cancer treatment. For instance, Wong Chadakul *et al.* (2018) developed a numerical model based on the finite element method (FEM) for thermal-mechanical deformation of 3-layered skin during laser-induced thermotherapy. They presented optimum skin treatment conditions by varying the wavelength, laser irradiation intensities, irradiation beam area, and blood perfusion rate [14]. Keangin *et al.* (2019) presented a simulation for liver cancer treated using a microwave coaxial antenna and included the deformation analysis to approach realistic tissue modeling [15].

Finally, all the mentioned aspects have a prominent role in the induced thermal damage in the treated tissue. The extensive research in this field demonstrates considerable interest in defining the predictive model for LA planning and evaluating the influencing parameters for therapy optimization [16]. Most of the mentioned studies focused on isolated aspects of the LA, and still today, the clinician's experience mainly guides the selection of the therapy settings. Indeed, the optimization of laser settings, including the mentioned influencing parameters, is still a missing step towards the safe use of laser therapy in clinical practice.

For the mentioned reasons, this work further supports LA optimization in the clinical setting by providing a decision-making strategy for cancer treatment based on the value of necrotic tissue and maximum temperature. So, to do this, a comprehensive mathematical model for predicting liver tissue behavior during the LA process was presented to reduce the undesirable side effects on healthy tissue and ensure cancerous tissue destruction. This procedure coupled two significant phenomena in which their governing equations are solved simultaneously. First, heat transfer based on the laser irradiation described by Beer-Lambert's law and Pennes' bioheat model to predict tissue temperature was applied [17]. The stress distribution in the tissue was predicted by using the equilibrium equation, the stress-strain relationship, and the strain displacement relationship [18]. Besides, the effect of the vessel on the process was investigated using laminar flow equations. The FEM was applied for solving the equations to analyze temperature changes in liver tissue. The temperature and thermal damage dependency of the optical properties of tissue, blood perfusion, heat capacity, tissue density, and thermal conductivity has been included in the simulation; when available, different properties for healthy tissue and tumor have been considered. The temperatures predicted by the model have been validated with experimental data. The effects of laser irradiation time, laser power, laser beam distribution, and blood vessel depth on temperature distribution were systematically studied and a set of optimum therapy settings was presented. The contributions of the present work are the thermomechanical analysis of soft tissues undergoing LA and the development of a comprehensive model intended for the preplanning stage for optimal cancer treatment. The outcome of this work is the first step towards a clinical application, in which specific patient's condition, such as a deep-seated tumor of irregular shape and surrounded by blood vessels of different diameters, should be considered.

II. MATERIAL AND METHODS

Time-dependent thermomechanical modeling equations and the initial and boundary conditions are solved simultaneously to investigate the laser-liver interaction. To simplify the model, the following assumptions are considered:

- 1) There is no chemical reaction.
- 2) A three-dimensional model is assumed.
- 3) Heat transfer is considered a time-dependent model.
- 4) The liver is assumed to be homogeneous and isotropic.
- 5) Laser absorption term in the tissue follows the Beer-Lambert's law.
- 6) The tumor geometry has an ellipsoid shape.

A. Thermomechanical Modeling of Laser Ablation Therapy

1) Bioheat Transfer Analysis: Many heat transfer models have been developed to describe the temperature distribution in laser-irradiated tissues. One of the most recognized models that predict heat transfer in biological tissues is Pennes's bioheat equation, which is based on the heat diffusion equation [19-25]. Here, a modified version that includes water vaporization in tissue was used [8]:

$$\rho C \frac{\partial T}{\partial t} = \nabla(k \nabla T) + \rho_b C_b \omega_b (T_b - T) + Q_{met} + Q_{laser} - Q_{vap} \quad (1)$$

where the left-hand side of (1) denotes the time-dependent term. The first, second, third, and fourth terms on the right-hand side denote heat conduction, heat dissipation by the blood flow, metabolic heat source (Q_{met}), and external heat source (Q_{laser}). The last term, Q_{vap} , is the energy needed to vaporize water. Also, C is the heat capacity of tissue (J/kg·K), ρ is the tissue density (kg/m³), k is the thermal conductivity of tissue (W/m·K), ρ_b is the density of blood (kg/m³), T is the tissue temperature (K), T_b is the temperature of blood (K), C_b is the specific heat capacity of blood (J/kg·K), ω_b is the blood perfusion rate (1/s).

Phase change process occurring at temperature around 100 °C is considered based on the formulation presented in [8]. The heat of water vaporization is a function of time:

$$Q_E = -\alpha \frac{dW}{dt} \quad (2)$$

where α is the water latent heat constant [kJ/kg] and W is the tissue water content [kg/m³].

From the chain rule, the derivative of concerning time is:

$$\frac{dW}{dt} = \frac{\partial W}{\partial T} \frac{\partial T}{\partial t} \quad (3)$$

$$Q_E = -\alpha \frac{\partial W}{\partial T} \frac{\partial T}{\partial t} \quad (4)$$

The modified bioheat equation then becomes:

$$\rho C_m \frac{\partial T}{\partial t} = \nabla(k \nabla T) + \rho_b C_b \omega_b (T_b - T) + Q_{met} + Q_{laser} \quad (5)$$

$$C_m = C - \frac{\alpha}{\rho} \cdot \frac{\partial W}{\partial T} = C - \frac{\alpha}{\rho} \cdot W'_T \quad (6)$$

where C_m is an effective specific heat, and water content W is a function of temperature [26]:

$$W(T) = 0.778 \times \begin{cases} 1 - \exp\left(\frac{T - 106}{3.42}\right) & T \leq 103^\circ C \\ 0.03713T^3 - 11.47T^2 + 1182T - 40582 & 103 < T \leq 104^\circ C \\ \exp\left(\frac{-T - 80}{34.37}\right) & T > 104^\circ C \end{cases} \quad (7)$$

Thermal conductivity of tissue in (5) is a function of temperature [27]–[31], as described in (8):

$$K(T) = \begin{cases} 0.5075 + 5.6261 \times 10^{-51} T^{25.296} & T \leq 100^\circ C \\ 55.44 - 0.99701T + 4.4988 \times 10^{-3} T^2 & T > 100^\circ C \end{cases} \quad (8)$$

The temperature dependency of the tissue density (ρ) is considered according to the following expression [31]:

$$\rho(T) = 1000 \cdot \{1.3 - 0.3 \cdot [1 - 4.98 \cdot 10^{-4} \cdot (T - 20)] \cdot w_m\} \quad (9)$$

in which w_m indicates the water mass percentage in liver tissue equal to ~69% [32].

Blood perfusion has a significant effect on heat transfer in *in vivo* ablation. Here, blood perfusion was considered a function of thermal tissue damage [33]:

$$\omega_b = \begin{cases} (1 + 25\Omega - 260\Omega^2)\omega_0 & 0 < \Omega \leq 0.1 \\ (1 - \Omega)\omega_0 & 0.1 < \Omega \leq 1 \end{cases} \quad (10)$$

where ω_0 is the perfusion rate in undamaged tissue, which is intended for tumor and healthy tissue separately. The first term of the equation reflects an initial increase in the perfusion rate as tissue is heated and vasodilation occurs. The second term shows that as the heating process continues and cell injury accumulates, blood flow decreases as the vasculature begins to shut down (thrombosis) [33], [34].

There is radiation in the tissue's upper surface and heat absorption from the laser irradiation at the laser beam spot.

$$-n \cdot (-k \nabla T) = \varepsilon \sigma (T_{am}^4 - T^4) \quad (11)$$

T_{am} is the ambient temperature (K), ε is surface emissivity, and σ is the Stefan–Boltzmann constant. Other boundaries are considered as a constant core body temperature ($T_b = 310.15$ K).

The laser irradiation is applied to the top surface of the tissue. Equation (12) describes the laser irradiance $I(z)$ (W/m²) [3]:

$$I(z) = I_0 e^{(-r^2/2\sigma^2)} \quad (12)$$

where r is the radial distance (mm), σ is the width of the irradiated area (mm), and I_0 is the irradiation intensity in the surface defined as:

$$I_0 = \frac{P}{2\pi\sigma^2} \quad (13)$$

where P indicates the laser power (W).

According to the Beer-Lambert's law, accounting absorption and scattering phenomena, the interaction of the laser light with biological can be expressed as [3]:

$$Q_{Laser} = \mu_{eff} I e^{-\mu_{eff} z} \quad (14)$$

where z is the depth of the tissue (m), and μ_{eff} is the effective attenuation coefficient (1/m), calculated as:

$$\mu_{eff} = \sqrt{3a(a + b(1 - g))} \quad (15)$$

in which a (1/m), b (1/m), and g are respectively the absorption, scattering, and anisotropy coefficients of tissue [35].

Given that the optical tissue properties vary during the ablation procedure due to the tissue temperature history and affect the thermal outcome, this dependency was implemented in the numerical model. This choice refers to the necessity to account for the variation of the optical properties to describe the laser-tissue interaction throughout the whole procedure.

The value $\Omega = 1$ was employed as a widely accepted criterion for representing tissue death [36]. Therefore, the optical properties can take values from the optical properties associated with native tissue to the optical properties associated with fully coagulated hepatic tissue [37]. Thus, the optical properties are defined by the following expressions:

$$a = a_{nat} \cdot (1 - \Omega) + a_{coag} \cdot \Omega \quad (16)$$

$$b = b_{nat} \cdot (1 - \Omega) + b_{coag} \cdot \Omega \quad (17)$$

$$g = g_{nat} \cdot (1 - \Omega) + g_{coag} \cdot \Omega \quad (18)$$

where Ω is thermal damage, a_{nat} (1/m), b_{nat} (1/m) and g_{nat} are respectively the absorptions, scattering, and anisotropy coefficients of native tissue, while a_{coag} (1/m), b_{coag} (1/m) and g_{coag} are the absorptions, scattering, and anisotropy coefficients of the coagulated tissue [38].

The geometry and the boundary conditions, and the physical domain are indicated in Fig. 1.

2) Thermal Injury Model: Thermal injury and cell necrosis can be evaluated using the Arrhenius equation [39], which estimates cell death as a function of temperature and exposure time [40]. The thermal injury can be approximated by a single process that is described by a first-order kinetics expression:

$$\Omega(t) = \ln \left(\frac{c(0)}{c(t)} \right) = \int_0^t A e^{-\frac{E}{RT}} dt \quad (19)$$

where $c(t)$ is the concentration of cells, $c(0)$ is the initial concentration of living cells, $\Omega(t)$ is the degree of tissue injury, R (J/(K.mol)) is the universal gas constant, T (K) is the absolute temperature, A is a frequency factor for the kinetic expression (1/s), and E is the activation energy for the irreversible damage (J/mol) [41].

3) Mechanical Deformation: Due to the temperature gradient in the heated exposed areas to laser irradiation, tissue deformation occurs in a realistic situation. For modeling the deformation, a simplified quasi-static model was considered in which an isotropic behavior was assumed for the tissue

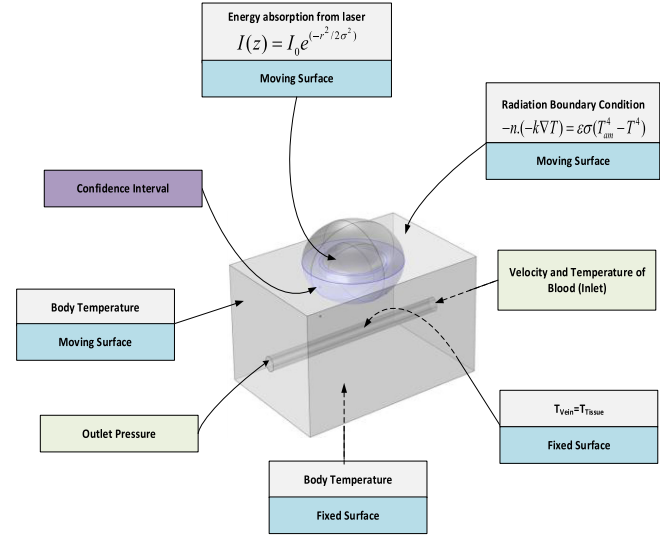


Fig. 1. Schematic view of the geometry of the healthy tissue, including tumor and blood vessel (i.e., the perfused case) and its boundary conditions.

[42]–[45]. The fundamental solid mechanic equations of an axisymmetric geometry can be described mathematically using the equilibrium equations, the stress-strain relationship, and the strain displacement relationship [46]:

$$\frac{\partial \sigma_{rr}}{\partial r} + \frac{\partial \sigma_{rz}}{\partial z} + \frac{\sigma_{rr} - \sigma_{\phi\phi}}{r} + F_r = 0 \quad (20)$$

$$\frac{\partial \sigma_{rz}}{\partial r} + \frac{\partial \sigma_{zz}}{\partial z} + \frac{\sigma_{rz}}{r} + F_r = 0 \quad (21)$$

$$\begin{cases} \varepsilon_{rr} = \frac{1}{E} [\sigma_{rr} - \nu(\sigma_{\phi\phi} + \sigma_{zz})] + \varepsilon^{th} \\ \varepsilon_{zz} = \frac{1}{E} [\sigma_{zz} - \nu(\sigma_{\phi\phi} + \sigma_{rr})] + \varepsilon^{th} \\ \varepsilon_{\phi\phi} = \frac{1}{E} [\sigma_{\phi\phi} - \nu(\sigma_{rr} + \sigma_{zz})] + \varepsilon^{th} \end{cases} \quad (22)$$

$$\begin{cases} \varepsilon_{rz} = \sigma_{rz}(1 + \nu)/E \\ \varepsilon_{rr} = \frac{\partial u_r}{\partial r}, \quad \varepsilon_{zz} = \frac{\partial u_z}{\partial z}, \quad \varepsilon_{\phi\phi} = \frac{u}{r} \\ \varepsilon_{rz} = \frac{1}{2} \left(\frac{\partial u_r}{\partial z} + \frac{\partial u_z}{\partial r} \right) \end{cases} \quad (23)$$

In the mentioned equations, E is Young's modulus (Pa), ν is the Poisson's ratio, σ denotes the stress (Pa), F is the external body load (Pa), and u is the average displacement (m). Moreover, the thermal strain (ε^{th}) is calculated by (24):

$$\varepsilon^{th} = \int_{T_{ref}}^T \alpha dT \quad (24)$$

where T_{ref} is the reference temperature and α is the tissue thermal expansion coefficient (1/K). The lower surface of the liver tissue is considered a fixed surface boundary condition, and the initial stress and strain are set to zero.

$$\begin{aligned} \sigma_{ri}, \sigma_{\phi i}, \sigma_{zi} \text{ and } \sigma_{rzi} &= 0 \\ \varepsilon_{ri}, \varepsilon_{\phi i}, \varepsilon_{zi} \text{ and } \varepsilon_{rzi} &= 0 \end{aligned}$$

The boundary condition for the mechanical deformation analysis is assumed to be free or fix for other surfaces.

If the heating effects are also taken into account, the relation between stress and strain for an isotropic material, in the existence of an external heating load can be expressed by the Duhamel–Neumann relation [47]:

$$\sigma_{ij} = \lambda e_{kk} \delta_{ij} + 2\mu e_{ij} - \beta\theta \quad (25)$$

where δ_{ij} is the Kronecker delta, θ is temperature excess over the ambient, e_{ij} is strain, λ is lame's constant, μ modulus of rigidity and β is a second-order tensor of thermoelastic moduli. This shows that in the absence of external mechanical loads, the stress tensor of the material decreases by increasing temperature, which certifies the stress not to exceed its yield value during the analysis.

4) Laminar Flow: In this study, blood is considered a Newtonian fluid, a common assumption in blood flow analysis. The maximum typical Reynolds number in the human body's vessel is 1980 [48], and this is below the critical Reynolds number in pipe [49]. Further, blood is assumed an incompressible, homogeneous fluid with an axisymmetric flow and constant viscosity. Under these assumptions, using a cylindrical coordinate system (r, θ, x), the complete 3-dimensional Navier-Stokes equations can be reduced to a set of 1-dimensional flow equations [50]:

$$\frac{\partial R}{\partial t} + V \frac{\partial R}{\partial x} + \frac{R}{2} \frac{\partial V}{\partial x} = 0 \quad (26)$$

$$\frac{\partial V}{\partial t} + 2(1 - \alpha) \frac{V}{R} \frac{\partial R}{\partial t} + \alpha V \frac{\partial V}{\partial x} + \frac{1}{\rho} \frac{\partial \rho_b}{\partial x} = \frac{\partial \nu}{R} \left[\frac{\partial \nu_x}{\partial r} \right]_R \quad (27)$$

where $R, V, \rho,$ and ν represent the inner vessel radius (m), average velocity (m/s), blood density (kg/m^3), and blood viscosity (m/s), respectively. The parameter α is used to specify the axial velocity profile's shape, with $\alpha = 1$ corresponding to a flat profile.

5) Model Geometry and Physical Constants: The geometry includes the healthy tissue, the tumor, and the vessel. Different meshing schemes were implemented, and the temperatures in the mesh elements were calculated to ensure that the solution is converged and independent of the mesh size. The result shows that by increasing the mesh resolution to 287323 elements, the temperature distribution in the tissue is reasonably independent of the number of mesh elements.

Information about tissue properties used in our model is available in Table I.

B. Experimental Setup

Fig. 2 shows the experimental setup in which the accuracy of the numerical model was verified with its experimental data. A porcine hepatic tissue underwent contactless LA, and simultaneous temperature monitoring was performed employing a network of fiber optic sensors.

The ablation was performed with a diode laser (LuOcean Mini 4, Lumics, Berlin, Germany) and the laser light was guided through a quartz optical fiber connected to a collimator (OZ Optics Ltd., Ottawa, Canada) and positioned perpendicularly at 5 cm from the liver surface. Three experiments in the same conditions (i.e., laser wavelength of 808 nm, laser beam diameter

TABLE I
THERMAL AND MECHANICAL PROPERTIES OF THE LIVER TISSUE, LASER IRRADIATION SETTING PARAMETERS, AND MODEL GEOMETRY

Parameter	Symbol	Value
Healthy tissue dimension (x, y, z)		40, 30, 20 mm
Ellipsoid tumor shape parameters [†]		a=4.5 mm, b=4.5 mm, c=2 mm
Vessel radius [51]		1 mm
Laser beam spot radius		5 mm
Laser power	P	2 - 10 W
Relative permeability of liver		1
Frequency factor [52]	A	5.51×10^{41} 1/s
Activation energy [52]	E	2.768×10^5 J/mol
Young's modulus of the liver [53]	E	1080 Pa
Young's modulus of the tumor [53]	E	12100 Pa
Poisson's ratio of the liver [54]	ν	0.3
The thermal expansion coefficient of the liver [55]	α	10^{-4} 1/K
Initial blood perfusion of liver [56]	ω_0	10^{-3}
Initial blood perfusion of tumor [56]	ω_0	0.91×10^{-3}
Density of blood [57]	ρ_b	1060 kg/m^3
Specific heat capacity of the blood [58]	C_b	3600 J/(kg °C)
Blood temperature	T_b	37 °C
Metabolic heat source [59]	Q_{met}	33.8 kW/m^3

[†]explained in Section III.B.

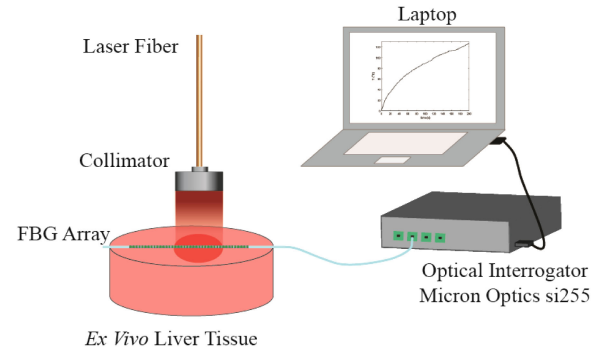


Fig. 2. Schematic view of contactless laser ablation set-up. The tissue temperature of the ex vivo porcine liver was measured by 40 fiber optic-based sensors embedded inside one fiber.

of 1 cm, laser power of 3.5 W and irradiation time of 200 s) have been repeated on three different regions of the liver. The ex vivo porcine liver was obtained from a local butcher and stored at 4 °C until the experiment was carried out. The starting temperature for the experiment was measured to be 19 °C. A network of 40 temperature sensors based on Fiber Bragg Grating (FBG) technology was used to measure the liver temperature increasing during laser irradiation. The FBG sensors were embedded in one optical fiber (contains an array of 40 FBGs), the sensing length of each FBG is 1.19 mm, and the edge-to-edge distance between close FBGs is 0.01 mm. A custom-made box was used to place the fiber on the surface. An optical spectrum interrogator (Micron Optics si255, Atlanta, USA, 1 pm accuracy corresponding to 0.1 °C) was used to interrogate the sensors and collect their optical output as a

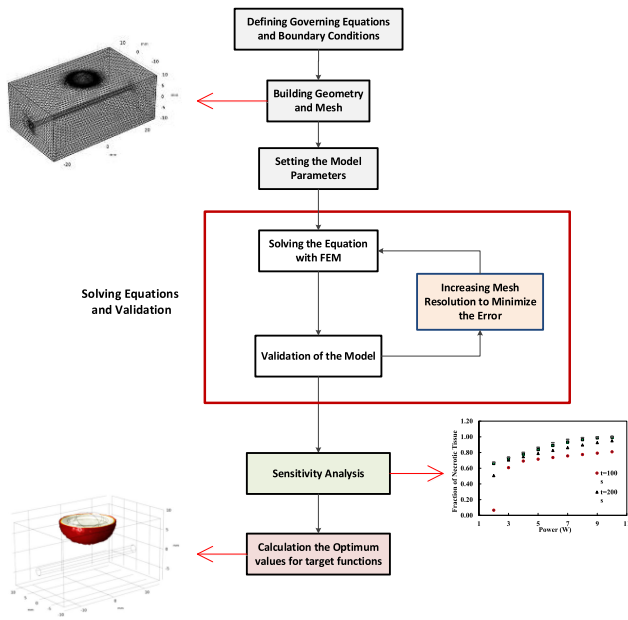


Fig. 3. Flowchart of the procedure design.

function of the tissue temperature. Details about the measurement systems can be found in previous works from the same group [60], [61].

C. Flowchart of the Designed Approach

In this work, the bioheat equation, deformed geometry equations, equilibrium equation, and related boundary conditions are numerically solved using the FEM. Fig. 3 presents the flowchart of the procedure designed and implemented in this work. Six steps can be identified in the flowchart; they are described as follows:

- Step (1): The governing equations and boundary conditions are specified.
- Step (2): The geometry is made according to assumptions and the experimental work.
- Step (3): All equations are solved simultaneously by using FEM.
- Step (4): The model is validated by comparing the simulation results with the experimental data.
- Step (5): Sensitivity analysis on laser irradiation time, laser power, laser beam distribution, and depth of vessel is performed to calculate the effect of each variable on the simulation results.
- Step (6): Optimum values for target functions are presented

III. RESULTS AND DISCUSSION

A. Validation of the Model

In order to perform the validation of the model, the geometry was considered as a simple shape to match the experimental set-up. Thus, neither the tumor nor the vessel was included in this step. Fig. 4(a) reports the trend of the average temperature measured by the sensor experiencing the maximum temperature

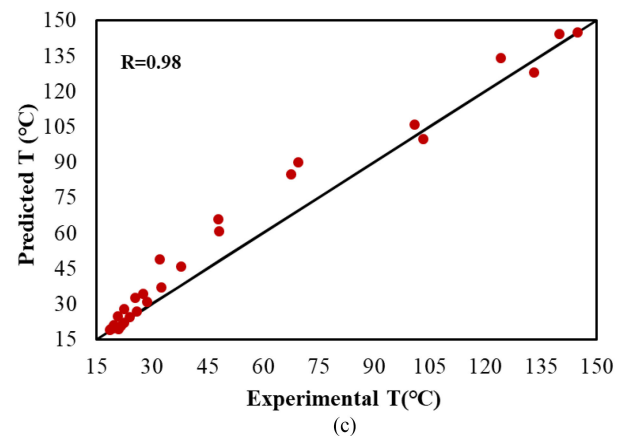
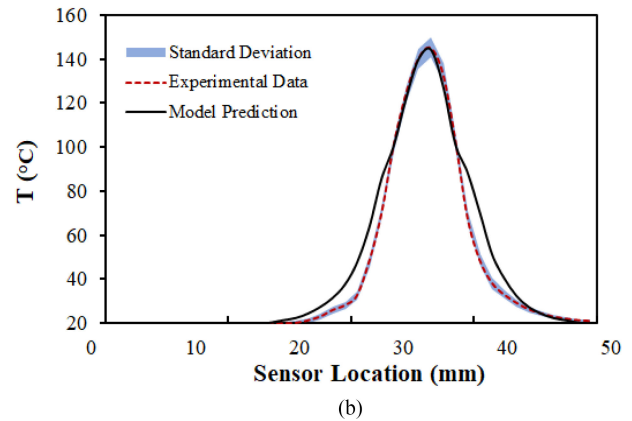
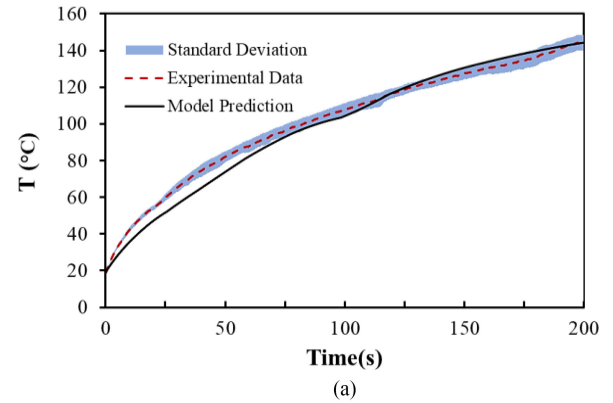


Fig. 4. (a) Temperature evolution measured on the surface of the tissue in the middle sensor during laser ablation. (b) Temperature distribution across the sensors after 200 s. (c) Comparison of the experimental data and predicted data in all sensors after 200 s.

increase (red dashed line), and the standard deviation calculated across the three measurements (light blue). The experimental results are compared with the temperature trend calculated by the implemented model (black curve), considering the same settings used in the experimental trials. The mean standard deviation is 3.1% along the whole trend, thus proving a limited variability across the experiments. Fig. 4(b) indicates the predicted temperature distribution of the sensors and the experimental data as a function of sensors along with the tissue after 200 s. The correlation factor, R , between the predicted and experimental

data after 200 s laser irradiation is 0.98 (Fig. 4(c)), and the mean absolute error is 3.9 °C, which shows a good performance.

Two significant changes have occurred in both the model prediction and experimental data, around 60 °C and 100 °C. The first one refers to the change of the tissue to the damaged one, as the effective attenuation coefficient increased in this condition. The second change corresponds to the water vaporization and thermal conductivity variation from 92 °C to 110 °C.

B. Perfused Model

In this section, the temperature distribution in the tumor and tissue, the amount of necrotic tissue, and stress distribution were calculated. The geometry of the tumor was considered as an ellipsoid with the following equation:

$$\frac{x^2}{a^2} + \frac{y^2}{b^2} + \frac{z^2}{c^2} = 1 \quad (28)$$

Furthermore, the dimensions are listed in Table I. In neoplasms with different dimensions, the model geometry should be accurately tuned to account for the tumor shape.

1) Von Mises Stress Distribution: Due to geometry irregularities, expectedly, stress concentration occurs in the boundary where tumor and vessel intersect (Fig. 5(a)). In this simulation, the thermal force causes this stress which has a direct relationship with the temperature. By moving away from this area, the stress decreases, and a stress jump occurs. Based on the principle of the Saint-Venant, by going far away from the heat source region, the effects of stress concentration disappear and start to stabilize throughout the tissue after a particular period [62]. Due to the energy equation, the average Von Mises stress in the contact line between tumor and healthy tissue approaches a steady state at around 100 s, as shown in Fig. 5(b). When the equilibrium state is reached, the heat transferred to the whole body, and the stress is instantly distributed through the tissue. The first principal stress is illustrated in Fig. 5(c), which explains the maximum stress within the liver. It is being noted that the maximum stress generated from the thermal loading is far less than the yield stress of the tissue [63], which guarantees that the liver stays in its elastic region.

2) Sensitivity Analysis: This section reports the sensitivity analysis performed to analyze the effect of influential variables on objective functions to optimize the LA process under certain specific conditions.

a) Effect of Laser Power and Ablation Time: Laser power and ablation time are the most crucial variable that significantly impacts the LA process [3]. Therefore, it's critical to look into their impact on temperature and the fraction of necrotic tissue, which are the main criterion for tumor destruction. As an example, Fig. 6 reports the fraction of necrotic tissue in the healthy liver and tumor exposed to a laser power of 7 W at irradiation time of 200 s:

To destroy cancerous tissue, the clinicians usually treat the so-called safety margins: they consider a small portion of healthy tissue around the tumor, which is usually removed to avoid undertreating undetectable tumor cells [64]. Here, a confidence interval with a thickness of 5 mm around the cancerous tumor

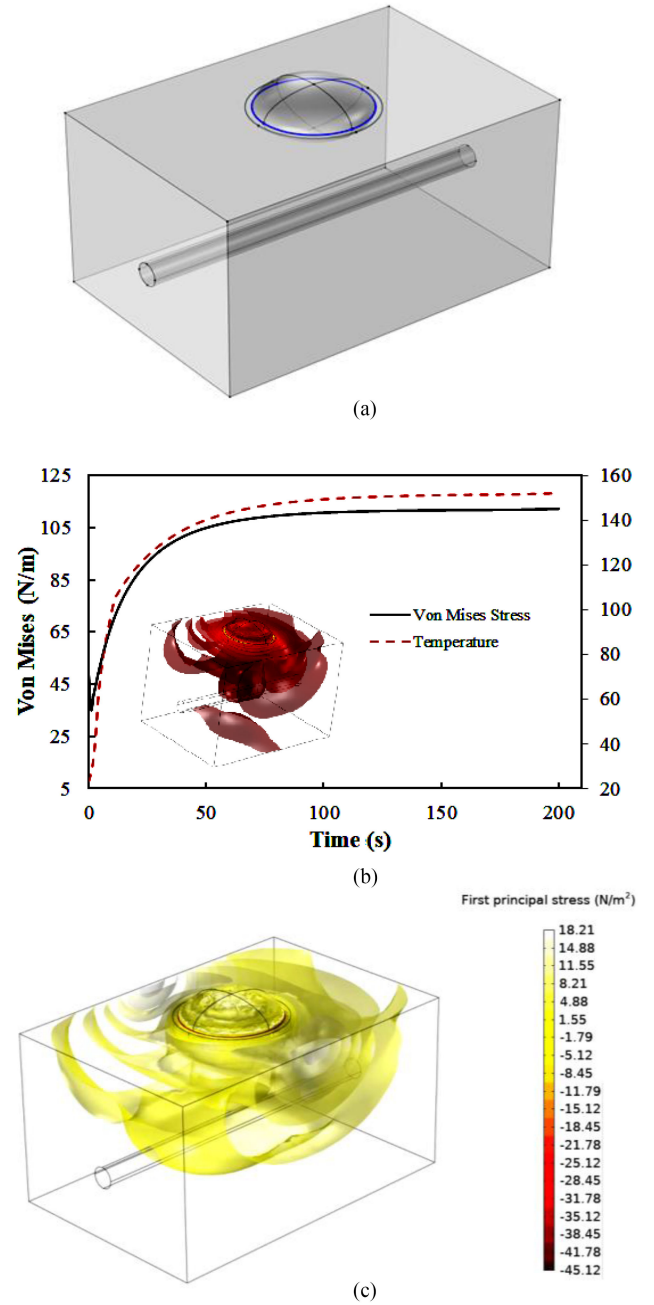


Fig. 5. (a) Detail of the line between the tumor and the healthy tissue at the geometry. (b) Average Von Mises stress, in the line between the tumor and healthy tissue and average temperature at this line. (c) Iosurface of first principal stress in the liver tissue and the tumor.

is considered, and the fraction of necrotic tissue was calculated in this safety margin.

The effect of the laser power and time on the perfused tissue (i.e., blood perfusion) is shown in Fig. 7. Here, laser power values of 2-10 W were considered, and the fraction of necrotic tissue and temperature in some parts of geometry were evaluated. Fig. 7(a) indicates the fraction of necrotic tissue, Fig. 7(b) reports the mean temperature in the tumor and the confidence interval and the maximum temperature at the power of 5 W and 200 s ablation time.

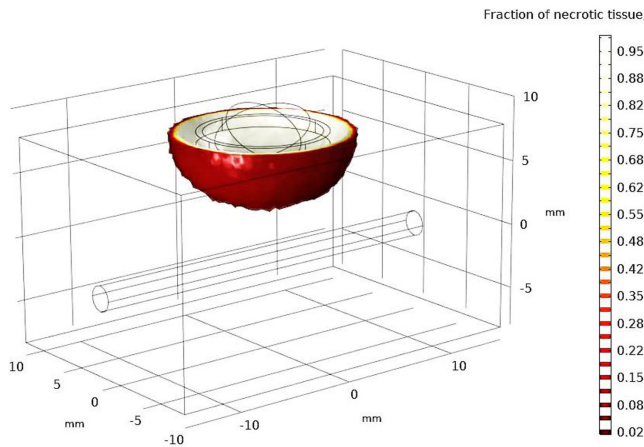


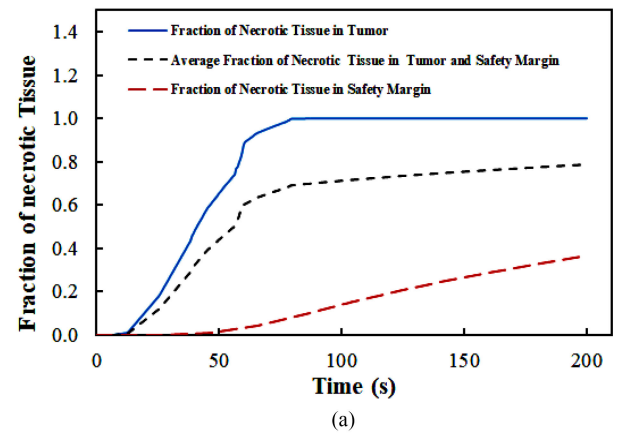
Fig. 6. Fraction of necrotic tissue after 200 s at 7 W in the perfused case.

The reduction of the laser power level leads to a reduction of necrotic tissue. Thus, appropriate settings are necessary for the treatment to be highly effective and to meet the highest safety standards and tumor destruction. Increasing the ablation time increased the fraction of necrotic tissue in the confidence interval, but, in a specific time, this value reaches a constant temperature, which occurs because other phenomena, like blood perfusion, dominates heat penetration.

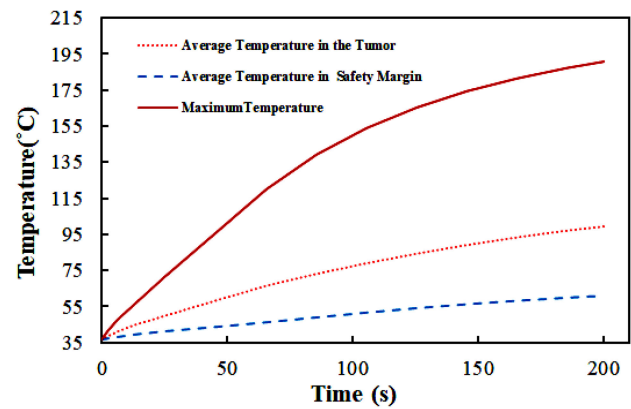
Fig. 7(c) shows the fraction of necrotic tissue *versus* laser power at different ablation times. The findings show that at constant power, the rate of necrotic tissue decreases with increasing ablation time; a similar effect is also accomplished with a fixed time and increased power. This study helps to define the ranges of these two variables for the optimization process.

b) Laser Power Distribution: The laser beam distribution at the power of 5 W is carried out in Fig. 8(a). This figure demonstrates the laser beam's power distribution, modeled as a gaussian distribution, at different standard deviations [9]. Considering two different locations in the model (point (1) and (2) in Fig. 8(b)), Fig. 8(c) shows the temperature values in these two points and for two different standard deviation values. When the laser distribution is tighter, the temperature at point (1) is higher. By increasing the standard deviation, the heat distributes more along the horizontal direction, then the temperature of this point decreased. As a result, with increasing standard deviation, the temperature difference between these two points was decreased, which is predictable due to the less focus of energy in the center of the laser beam. Moreover, in correspondence with point (1), it is possible to observe that increasing the standard deviation from 1 to 5 mm corresponds to a decrease of the maximum temperature of more than 50 °C. Considering that the temperature evolutions and gradients are responsible for the final thermal damage induced in the tissue, the analysis of the size of the beam distribution is relevant [65].

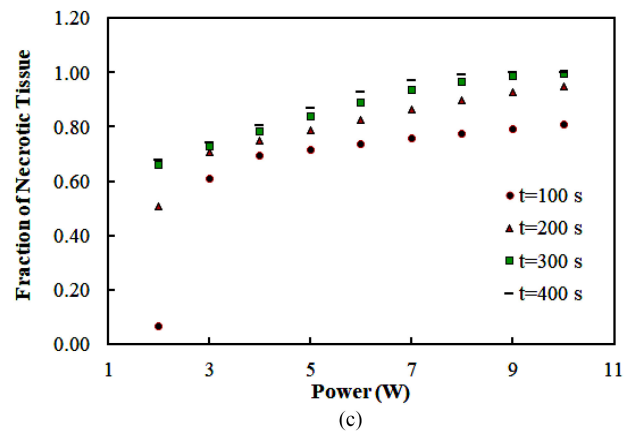
c) Effect of the Blood Vessel on the Heat Transfer: In this section, a blood vessel was added to the simulation, and its effect was investigated. Indeed, Pennes' bioheat equation (1) can accurately predict the heat transfer by small capillaries, but it cannot assess the heat sink effect caused by large vessels.



(a)



(b)



(c)

Fig. 7. (a) The fraction of necrotic tissue in the tumor and safety margin. (b) the average temperature in tumor and safety margin, and maximum temperature in the tissue versus ablation time at a laser power of 5 W. (c) The fraction of necrotic tissue and safety margin versus laser irradiation power at different ablation time.

Hence, including the blood vessel in the simulation may improve the prediction capability [23], [66]. Fig. 9(a) shows the vessel's effect in terms of the unsymmetric shape of temperature distribution. The temperature in two specific tissue coordinates as a function of vessel depth is assessed in Fig. 9(c). Fig. 9(b) shows the placement of the two selected points, i.e., point (1), close to the vessel inlet, and point (2), close to the outlet. When the vessel is far from the tissue surface (which means a distance from the tumor boundary >5 mm), it has no effect on heat transfer

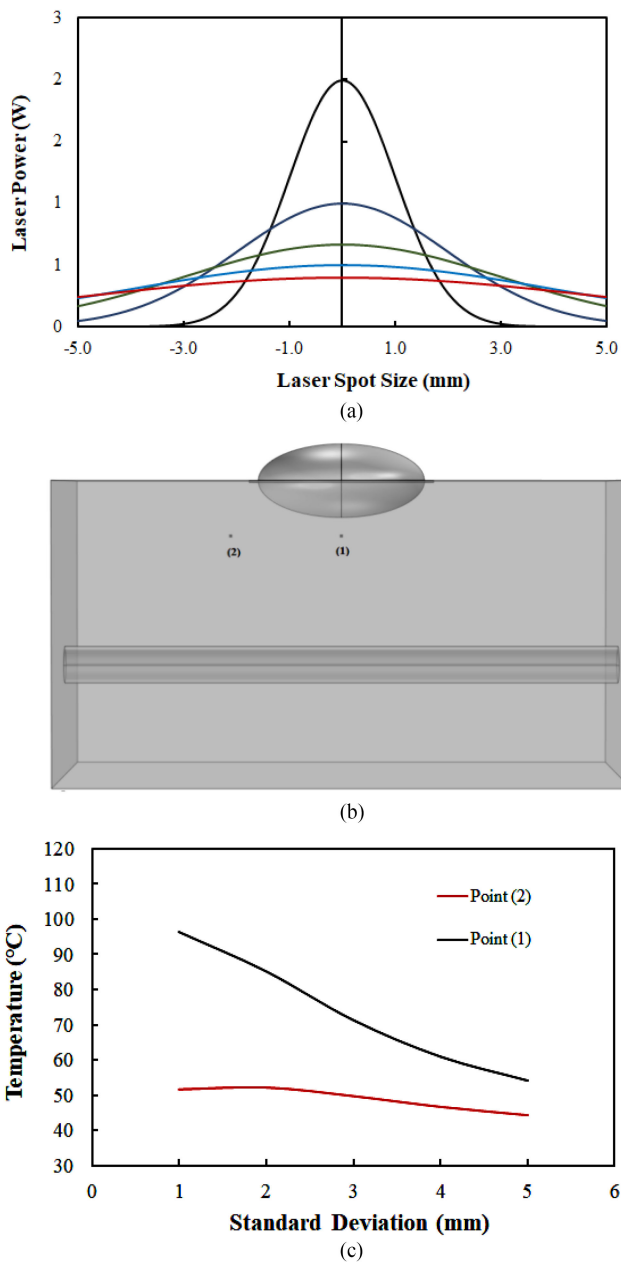


Fig. 8. (a) Laser power distribution in different standard deviation, (b) two points where the temperature distribution evaluated, and (c) temperature with different laser beam distribution at two points at 200 s and power 5 W.

from the laser to the two points (at a fixed irradiation time and laser power). Its effect appears by reducing this distance to 7 mm (which means a distance from the tumor of 5 mm). At point (1), which is the closest to the vessel inlet, the temperature is lower because fresh blood (initial temperature is 37 °C) enters the vessel at a lower temperature and has heat transfer with the tissue. When the depth of the vessel decreased, this effect is more evident. Indeed, the temperature in the tissue region close to the vessel inlet, point (1), results to be ~5 °C lower than the outlet temperature at point (2), when the vessel is at 5 mm distance from the tissue surface (i.e., 3 mm distance from the tumor boundary).

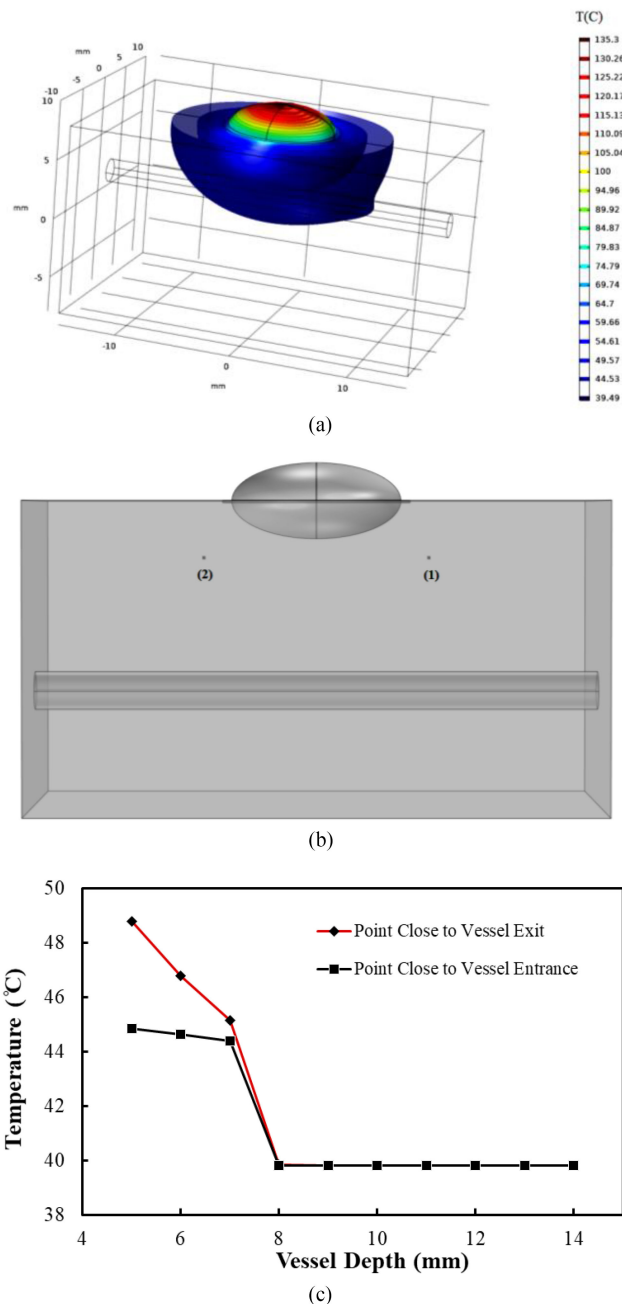


Fig. 9. (a) Temperature distribution in the presence of the vessel (200 s and 5 W). (b) Two points to evaluate the effect of the vessel position on the temperature: point (1), close to the vessel inlet, and point (2), close to the outlet. (c) The temperature in two probe points as a function of vessel depth.

C. Optimization

During thermal ablation, a high and uncontrolled temperature could lead to undesired thermal damage in the tissue. Therefore, it is necessary to assess how both the temperature and the necrotic tissue increase. The operator must reach a specific amount of tissue destruction to ensure that the tumor is destroyed. The extent to which the temperature and necrotic fraction increase during laser-induced thermotherapy predominantly depends on the irradiation time and the laser

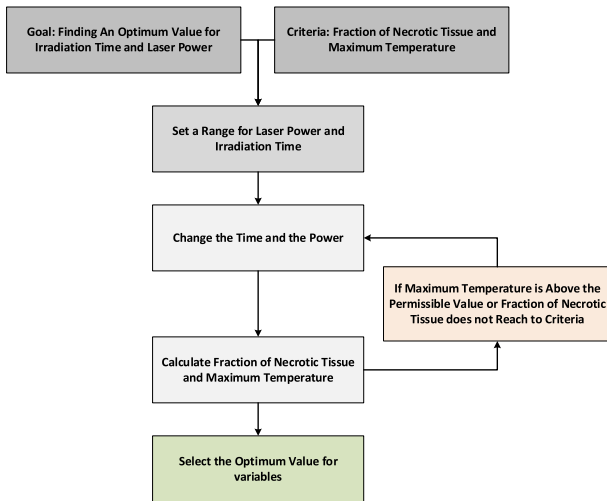


Fig. 10. The flowchart including steps of the decision-making and optimization processes.

irradiation power. Here, these two variables, which correspond to the clinical settings, were considered independent variables in the optimization process. The objective functions are the amount of necrotic tissue in a confidence interval and tumor, and the maximum temperature. The experience of experts and previous information on the biological effects of temperature were used to select the value of final independent variables in the decision-making process based on the objective functions.

In this optimization analysis, the safety margin of 5 mm was considered as a confidence interval to ensure that the tumor is destroyed during the LA. This choice is made in agreement with clinicians’ opinions [67]. Based on this criterion, a proposed decision-making process, and a bunch of values for irradiation time and laser power were presented. Fig. 10 sketches the decision-making process, which involves the following steps:

- Goal: To get the best values for the independent variables.
- Step (1): Selecting maximum temperature and the average fraction of necrotic tissue in the confidence interval and tumor as the objective functions.
- Step (2): Setting a range for independent variables.
- Step (3): Calculating the objective functions for all sets of independent variables.
- Step (4): Choosing a set of independent variables based on objective functions criterion.

The values of two independent variables were changed in the range obtained from the sensitivity analysis, and the values of the two target variables were obtained. In general, the higher the power, the lower the time needed to achieve a similar fraction of necrotic tissue inside the safety margins.

Table II(a) shows part of the results for the fraction of necrotic tissue in the confidence interval and tumor with each independent time and power set. The fraction of necrotic tissue reached a constant value with increasing time in some cases. This phenomenon indicates that at a constant value of the laser power, the rate of necrotic tissue growth in the tissue dramatically decreased. Considering the presented geometry, we hypothesize that an optimal procedure should bring a percent amount of

TABLE II
OPTIMIZATION RESULTS; A) FRACTION OF NECROTIC TISSUE, B) MAXIMUM TEMPERATURE.

(a) Average Fraction of Necrotic Tissue in Tumor and Confidence Interval

		Time (s)									
		50	100	150	200	250	300	350	400	450	500
Power (W)	2	0.000	0.066	0.301	0.506	0.613	0.661	0.674	0.677	0.681	0.682
	3	0.193	0.608	0.687	0.705	0.719	0.728	0.735	0.739	0.744	0.749
	4	0.491	0.692	0.723	0.748	0.767	0.782	0.792	0.802	0.811	0.813
	5	0.660	0.715	0.755	0.789	0.816	0.837	0.854	0.867	0.884	0.895
	6	0.682	0.737	0.785	0.827	0.861	0.890	0.910	0.925	0.938	0.949
	7	0.695	0.757	0.813	0.863	0.904	0.934	0.952	0.968	0.978	0.986
	8	0.706	0.774	0.839	0.897	0.939	0.964	0.981	0.990	0.995	0.996
	9	0.715	0.799	0.864	0.927	0.964	0.987	0.994	0.997	0.999	1.000
	10	0.725	0.809	0.888	0.950	0.983	0.996	0.998	1.000	1.000	1.000

(b) Maximum Temperature

		Time (s)									
		50	100	150	200	250	300	350	400	450	500
Power (W)	2	53.9	59.2	71.2	80.4	84.5	87.3	89.1	89.6	90.5	90.6
	3	69.2	94.9	107.6	116.0	121.8	125.4	127.6	128.9	130.2	131.4
	4	92.0	123.8	143.0	154.6	162.1	166.7	169.6	171.8	173.7	173.8
	5	110.9	153.7	177.1	190.8	199.5	205.2	209.1	211.6	214.2	215.9
	6	132.2	183.2	209.8	225.8	235.8	242.2	246.8	249.8	252.7	254.7
	7	153.5	211.5	241.5	259.1	270.2	277.7	282.8	286.3	289.1	291.5
	8	173.8	238.8	272.2	291.2	303.3	311.6	316.8	320.7	324.0	326.3
	9	194.4	265.7	301.8	322.1	335.1	343.8	349.4	353.6	357.1	359.4
	10	214.6	292.1	330.4	351.8	365.5	374.4	380.3	384.6	388.0	390.7

necrotic tissue of at least 80%. The tissue’s maximum temperature is shown as another criterion for selecting the optimal conditions in Table II(b). We also introduce a criterion for the tissue temperature, which should not go beyond 200 °C, since carbonization is typically associated with this value, together with other potential complications [68]. Indeed, the procedure should be performed at the lowest temperature as possible to guarantee the safety of the treatment and, at the same time, efficacy for tumor destruction. Finally, according to the proposed criteria and an expert opinion who performs the surgery once the decision-making process has been completed, two independent variables (i.e., power and time) should be selected.

In Table II (a), the optimal values are selected based on the fraction of necrotic in the confidence interval has reached over 80%. In Table II(b), some data are removed according to the temperature criterion because the temperature is above 200 °C. Due to this percentage of tissue destruction and temperatures, the thermal procedure can be successfully performed in our modeling conditions.

Fig. 11 shows the optimal front, which is the output of the optimization process. The values outside of this front are not optimum. According to the tumor size and modeling conditions, the maximum and minimum values for laser power and laser irradiation time is presented in this figure.

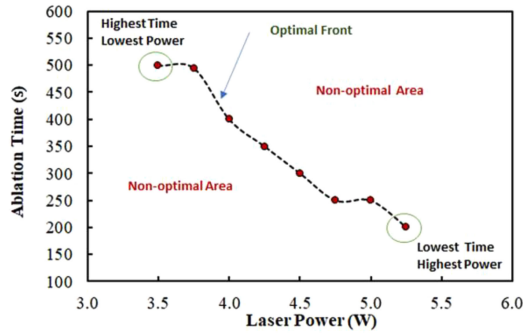


Fig. 11. The optimal frontier for laser power and ablation time.

It is noteworthy to indicate that the optimal values proposed in the optimization section refer to the specific geometry and conditions implemented in our analysis. The proposed workflow and implementation should be adapted to specific cases and tumor and tissue geometry and conditions during the treatment preplanning. Even though our work includes the thermal-dependency of the thermal, mechanical, and optical properties of the tissue and tumor, when available, the patient-specific conditions should be considered during an optimization procedure for a clinical application. For instance, the position of the tumor inside the organ and its irregular shape should be taken into account, together with the pattern of the significant blood vessel surrounding the target zone. However, our model has been satisfactorily validated by experimental data. Although the experimental configuration used in this work is far from the clinical scenario, it enables an accurate control in sensors positioning, power distribution, and thermal outcome. This control is necessary to perform the validation of the proposed model in a preliminary step of the analysis. Indeed, the final goal of the proposed model is to streamline the therapy planning stage by performing the first step of the decision-making process. The proposed model could represent a valid tool to guide the clinician through a thorough decision-making process based on the numerical modeling results.

IV. CONCLUSION

This work presents transient numerical modeling to predict the behavior of contactless LA under various conditions. Based on the proposed approach, a thermomechanical model was developed and validated with experimental data (i.e., porcine liver tissue) to illustrate its effectiveness and suitability. The most influential variables affecting the ablative phenomenon were identified, which became the laser power and exposure time. From these observations, an optimization process has been carried out to identify the most appropriate procedural settings for effectively treating the tumor while assuring a safety margin surrounding the lesion. This work lays the foundations for developing a therapy planning platform to guide the clinician in selecting the proper therapy parameters. In light of recent advances in diagnostic imaging techniques, future studies should focus on the patient-specific geometry to consider the actual tumor size, location, and shape.

ACKNOWLEDGMENT

The authors would like to acknowledge Alexey Wolf and Alexander Dostovalov at the Department of Physics, Novosibirsk State University and the Institute of Automation and Electrometry, Siberian Branch of the Russian Academy of Sciences, Novosibirsk, Russia for producing the fiber Bragg grating sensors mentioned in this work.

REFERENCES

- [1] L. Goldman, *The Biomedical Laser: Technology and Clinical Applications*. Berlin, Germany: Springer, 2013.
- [2] E. Schena *et al.*, "Laser ablation for cancer: Past, present and future," *J. Funct. Biomater.*, vol. 8, no. 2, 2017, Art. no. 19.
- [3] P. Saccomandi *et al.*, "Theoretical analysis and experimental evaluation of laser-induced interstitial thermotherapy in ex vivo porcine pancreas," *IEEE Trans. Biomed. Eng.*, vol. 59, no. 10, pp. 2958–2964, Oct. 2012.
- [4] C. Rossmann and D. Haemmerich, "Review of temperature dependence of thermal properties, dielectric properties, and perfusion of biological tissues at hyperthermic and ablation temperatures," *Crit. Rev. Biomed. Eng.*, vol. 42, no. 6, pp. 467–492, 2014.
- [5] S. Singh *et al.*, "Sensitivity analysis of critical parameters affecting the efficacy of microwave ablation using taguchi method," *Int. J. RF Microw. Comput.-Aided Eng.*, vol. 29, no. 4, 2019, Art. no. e21581.
- [6] G. J. Müller and A. Roggan, *Laser-Induced Interstitial Thermotherapy*. Bellingham, WA USA: SPIE Press, 1995.
- [7] K. Kulikov, *Laser Interaction With Biological Material*. Berlin, Germany: Springer, 2016.
- [8] D. Yang *et al.*, "Expanding the bioheat equation to include tissue internal water evaporation during heating," *IEEE Trans. Biomed. Eng.*, vol. 54, no. 8, pp. 1382–1388, Aug. 2007.
- [9] S. Blauth *et al.*, "Mathematical modeling of vaporization during laser-induced thermotherapy in liver tissue," *J. Math. Ind.*, vol. 10, pp. 1–16, 2020.
- [10] T.-C. Shih *et al.*, "Cooling effect of thermally significant blood vessels in perfused tumor tissue during thermal therapy," *Int. Commun. Heat Mass Transfer*, vol. 33, no. 2, pp. 135–141, 2006.
- [11] A. Shirkavand and H. R. Nazif, "Numerical study on the effects of blood perfusion and body metabolism on the temperature profile of human forearm in hyperthermia conditions," *J. Thermal Biol.*, vol. 84, pp. 339–350, 2019.
- [12] S. Singh and R. Melnik, "Thermal ablation of biological tissues in disease treatment: A review of computational models and future directions," *Electromagn. Biol. Med.*, vol. 39, no. 2, pp. 49–88, 2020.
- [13] J. Zhang *et al.*, "Towards real-time finite-strain anisotropic thermo-viscoelastodynamic analysis of soft tissues for thermal ablative therapy," *Comput. Methods Programs Biomed.*, vol. 198, 2021, Art. no. 105789.
- [14] P. Wongchadukul *et al.*, "Implementation of a thermomechanical model to simulate laser heating in shrinkage tissue (effects of wavelength, laser irradiation intensity, and irradiation beam area)," *Int. J. Thermal Sci.*, vol. 134, pp. 321–336, 2018.
- [15] P. Keangin *et al.*, "Analysis of heat transfer in deformed liver cancer modeling treated using a microwave coaxial antenna," *Appl. Thermal Eng.*, vol. 31, no. 16, pp. 3243–3254, 2011.
- [16] S. Asadi, L. Bianchi, M. De Landro, S. Korganbayev, E. Schena, and P. Saccomandi, "Laser-induced optothermal response of gold nanoparticles: From a physical viewpoint to cancer treatment," *J. Biophotonics*, vol. 14, no. 2, 2021, Art. no. e202000161.
- [17] H. H. Pennes, "Analysis of tissue and arterial blood temperatures in the resting human forearm," *J. Appl. Physiol.*, vol. 85, no. 1, pp. 5–34, 1998.
- [18] B. Rubinsky, "Thermal stresses during solidification processes," *J. Heat Transfer*, vol. 104, pp. 196–199, 1982.
- [19] H. Arkin, L. X. Xu, and K. R. Holmes, "Recent developments in modeling heat transfer in blood perfused tissues," *IEEE Trans. Biomed. Eng.*, vol. 41, no. 2, pp. 97–107, Feb. 1994.
- [20] M. Jaunich *et al.*, "Bio-heat transfer analysis during short pulse laser irradiation of tissues," *Int. J. Heat Mass Transfer*, vol. 51, no. 23/24, pp. 5511–5521, 2008.
- [21] E. Ng *et al.*, "Prediction and parametric analysis of thermal profiles within heated human skin using the boundary element method," *Philos. Trans. Roy. Soc. A: Math., Phys. Eng. Sci.*, vol. 368, no. 1912, pp. 655–678, 2010.

- [22] T. Wessapan *et al.*, "Numerical analysis of specific absorption rate and heat transfer in the human body exposed to leakage electromagnetic field at 915 MHz and 2450 MHz," *J. Heat Transfer*, vol. 133, no. 5, 2011, Art. no. 051101.
- [23] A. Paul *et al.*, "Temperature evolution in tissues embedded with large blood vessels during photo-thermal heating," *J. Thermal Biol.*, vol. 41, pp. 77–87, 2014.
- [24] R. Dua and S. Chakraborty, "A novel modeling and simulation technique of photo-thermal interactions between lasers and living biological tissues undergoing multiple changes in phase," *Comput. Biol. Med.*, vol. 35, no. 5, pp. 447–462, 2005.
- [25] X. Wu *et al.*, "Theoretical and experimental study of dual-fiber laser ablation for prostate cancer," *PLoS One*, vol. 13, no. 10, 2018, Art. no. e0206065.
- [26] D. Yang *et al.*, "Measurement and analysis of tissue temperature during microwave liver ablation," *IEEE Trans. Biomed. Eng.*, vol. 54, no. 1, pp. 150–155, Jan. 2006.
- [27] V. Lopresto *et al.*, "Temperature dependence of thermal properties of ex vivo liver tissue up to ablative temperatures," *Phys. Med. Biol.*, vol. 64, no. 10, 2019, Art. no. 105016.
- [28] N. P. Silva *et al.*, "Characterisation of ex vivo liver thermal properties for electromagnetic-based hyperthermic therapies," *Sensors*, vol. 20, no. 10, 2020, Art. no. 3004.
- [29] A. Bhattacharya and R. Mahajan, "Temperature dependence of thermal conductivity of biological tissues," *Physiol. Meas.*, vol. 24, no. 3, 2003, Art. no. 769.
- [30] D. Haemmerich *et al.*, "In vitro measurements of temperature-dependent specific heat of liver tissue," *Med. Eng. Phys.*, vol. 28, no. 2, pp. 194–197, 2006.
- [31] S. R. Guntur *et al.*, "Temperature-dependent thermal properties of ex vivo liver undergoing thermal ablation," *Ultrasound Med. Biol.*, vol. 39, no. 10, pp. 1771–1784, 2013.
- [32] Y. Mohammed and J. F. Verhey, "A finite element method model to simulate laser interstitial thermo therapy in anatomical inhomogeneous regions," *Biomed. Eng. Online*, vol. 4, no. 1, pp. 1–16, 2005.
- [33] J. Abraham and E. Sparrow, "A thermal-ablation bioheat model including liquid-to-vapor phase change, pressure-and necrosis-dependent perfusion, and moisture-dependent properties," *Int. J. Heat Mass Transfer*, vol. 50, no. 13/14, pp. 2537–2544, 2007.
- [34] S. A. Baldwin *et al.*, "A heat transfer model of thermal balloon endometrial ablation," *Ann. Biomed. Eng.*, vol. 29, no. 11, pp. 1009–1018, 2001.
- [35] A. Ishimaru, "Diffusion of light in turbid material," *Appl. Opt.*, vol. 28, no. 12, pp. 2210–2215, 1989.
- [36] F. Kreith, and R. P. Chhabra, *CRC Handbook of Thermal Engineering*. Boca Raton, FL, USA: CRC press, 2017.
- [37] J. P. Ritz *et al.*, "Optical properties of native and coagulated porcine liver tissue between 400 and 2400 nm," *Lasers Surg. Med.: Official J. Amer. Soc. Laser Med. Surg.*, vol. 29, no. 3, pp. 205–212, 2001.
- [38] T. H. Nguyen *et al.*, "Temperature feedback-controlled photothermal treatment with diffusing applicator: Theoretical and experimental evaluations," *Biomed. Opt. Exp.*, vol. 7, no. 5, pp. 1932–1947, 2016.
- [39] I. A. Chang and U. D. Nguyen, "Thermal modeling of lesion growth with radiofrequency ablation devices," *Biomed. Eng. Online*, vol. 3, no. 1, pp. 1–19, 2004.
- [40] R. J. Stafford *et al.*, "Laser-induced thermal therapy for tumor ablation," *Crit. Rev. Biomed. Eng.*, vol. 38, no. 1, pp. 79–100, 2010.
- [41] M. Borrelli *et al.*, "Time-temperature analysis of cell killing of BHK cells heated at temperatures in the range of 43.5 C to 57.0 C," *Int. J. Radiat. Oncol. Biol. Phys.*, vol. 19, no. 2, pp. 389–399, 1990.
- [42] S. Lin *et al.*, "Thermal stresses induced by water solidification in a cylindrical tube," *J. Heat Transfer (Trans. ASME (Amer. Soc. Mech. Engineers), Ser. C); (United States)*, vol. 112, no. 4, pp. 1079–1082, 1990.
- [43] S. Nemat-Nasser, *Plasticity: A Treatise on Finite Deformation of Heterogeneous Inelastic Materials*. Cambridge, U.K.: Cambridge Univ. Press, 2004.
- [44] C. Thornton and S. Antony, "Quasi-static deformation of particulate media," *Philos. Trans. Roy. Soc. London. Ser. A: Math., Phys. Eng. Sci.*, vol. 356, no. 1747, pp. 2763–2782, 1998.
- [45] A. De Koning, "A contribution to the analysis of quasi static crack growth in sheet materials," in *Proc. 4th Int. Conf. Fracture Anal. Mech.*, Amsterdam, The Netherlands; New York: Elsevier, 1978, pp. 25–31.
- [46] B. A. Boley and J. H. Weiner, *Theory of Thermal Stresses*. North Chelmsford, Chelmsford, MA, USA: Courier Corporation, 2012.
- [47] B. Das, *Problems and Solutions in Thermoelasticity and Magneto-Thermoelasticity*. Berlin, Germany: Springer, 2017.
- [48] E. Helps and D. McDonald, "Observations on laminar flow in veins," *J. Physiol.*, vol. 124, no. 3, 1954, Art. no. 631.
- [49] C. Vlachopoulos, M. O'Rourke, and W. W. Nichols, *McDonald's Blood Flow in Arteries: Theoretical, Experimental and Clinical Principles*. Boca Raton, FL, USA: CRC press, 2011.
- [50] T. D. Maboutwana *et al.*, "A model of blood flow in the mesenteric arterial system," *Biomed. Eng. Online*, vol. 6, no. 1, pp. 1–12, 2007.
- [51] R. Ma *et al.*, "Anatomically based simulation of hepatic perfusion in the human liver," *Int. J. Numer. Methods Biomed. Eng.*, vol. 35, no. 9, 2019, Art. no. e3229.
- [52] E. G. Macchi *et al.*, "Dielectric properties of RF heated ex vivo porcine liver tissue at 480 kHz: Measurements and simulations," *J. Phys. D: Appl. Phys.*, vol. 47, no. 48, 2014, Art. no. 485401.
- [53] W.-C. Yeh *et al.*, "Elastic modulus measurements of human liver and correlation with pathology," *Ultrasound Med. Biol.*, vol. 28, no. 4, pp. 467–474, 2002.
- [54] Y. Hirahara *et al.*, "Development of liver injury simulation model using MPS method," in *Proc. Int. Conf. Model. Simul. Appl. Math.*, 2015, pp. 250–252.
- [55] B. Soroushian *et al.*, "Study of laser-induced thermoelastic deformation of native and coagulated ex-vivo bovine liver tissues for estimating their optical and thermomechanical properties," *J. Biomed. Opt.*, vol. 15, no. 6, 2010, Art. no. 065002.
- [56] Y. Yin *et al.*, "Characteristic analysis of light and heat transfer in photothermal therapy using multiple-light-source heating strategy," *Int. J. Thermal Sci.*, vol. 158, 2020, Art. no. 106533.
- [57] T. Kenner, "The measurement of blood density and its meaning," *Basic Res. Cardiol.*, vol. 84, no. 2, pp. 111–124, 1989.
- [58] K. A. Rosentrater and R. A. Flores, "Physical and rheological properties of slaughterhouse swine blood and blood components," *Trans. ASAE*, vol. 40, no. 3, pp. 683–689, 1997.
- [59] Y. Rabin and A. Shitzer, "Numerical solution of the multidimensional freezing problem during cryosurgery," *J. Biomech. Eng.*, vol. 120, pp. 32–37, 1998.
- [60] F. Morra *et al.*, "Spatially resolved thermometry during laser ablation in tissues: Distributed and quasi-distributed fiber optic-based sensing," *Opt. Fiber Technol.*, vol. 58, 2020, Art. no. 102295.
- [61] S. Korganbayev *et al.*, "Closed-loop temperature control based on fiber bragg grating sensors for laser ablation of hepatic tissue," *Sensors*, vol. 20, no. 22, 2020, Art. no. 6496.
- [62] R. L. Cooley and S. A. Moin, "Finite element solution of saint-venant equations," *J. Hydraul. Division*, vol. 102, no. 6, pp. 759–775, 1976.
- [63] A. Karimi and A. Shojaei, "An experimental study to measure the mechanical properties of the human liver," *Dig. Dis.*, vol. 36, no. 2, pp. 150–155, 2018.
- [64] Y.-S. Kim *et al.*, "The minimal ablative margin of radiofrequency ablation of hepatocellular carcinoma (>2 and < 5 cm) needed to prevent local tumor progression: 3D quantitative assessment using CT image fusion," *Amer. J. Roentgenol.*, vol. 195, no. 3, pp. 758–765, 2010.
- [65] A. J. Welch and M. J. Van Gemert, *Optical-Thermal Response of Laser-Irradiated Tissue*. Berlin, Germany: Springer, 2011.
- [66] A. Paul and A. Paul, "Computational study of photo-thermal ablation of large blood vessel embedded tumor using localized injection of gold nanoshells," *J. Thermal Biol.*, vol. 78, pp. 329–342, 2018.
- [67] J. Schaible *et al.*, "Safety margin assessment after microwave ablation of liver tumors: Inter-and intrareader variability," *Radiol. Oncol.*, vol. 1, pp. 57–61, 2020.
- [68] S. Thomsen and J. Pearce, "Thermal damage and rate process in biological tissues," in *Optical Thermal Response of Laser Irradiated Tissue*, 2nd ed., A. J. Welch and M. J. C. Van Gemert, Eds., The Netherlands: Springer, Dordrecht, 2011.